RSC Advances

PAPER

View Article Online
View Journal | View Issue

Cite this: *RSC Adv.*, 2023, **13**, 17923

Structural, dielectric and transport properties of $Na_xFe_{1/2}Mn_{1/2}O_2$ ($x = 1$ and 2/3)†

Faouzi Missaoui,[a] Kawthar Trablsi,[a] Krimi Moufida,[a] Ayten Ates,[b] Abdelfattah Mahmoud,[c] Frédéric Boschini[c] and Abdallah Ben Rhaiem *[a]

$Na_xFe_{1/2}Mn_{1/2}O_2$ ($x = 1$ and 2/3) layered oxides were prepared by an improved solid-state synthesis method. The XRD analysis confirmed the high purity of these samples. The Rietveld refinement of the crystalline structure illustrated that the prepared materials crystallize in a hexagonal system in the $R\bar{3}m$ space group with the P3 structure for $x = 1$ and in a rhombohedral system with the $P6_3/mmc$ space group and P2 structure type for $x = 2/3$. The vibrational study undertaken using IR and Raman spectroscopy techniques yielded the existence of an MO_6 group. Their dielectric properties were determined in frequency range 0.1–10^7 Hz for a temperature range 333–453 K. The permittivity results indicated the presence of two types of polarization, namely dipolar polarization and space charge polarization. The frequency dependence of the conductivity was interpreted in terms of Jonscher's law. The DC conductivity followed the Arrhenius laws either at low or at high temperatures. The temperature dependence of the power law exponent which corresponds to the grain (s_2) suggested that the conduction of the P3-$NaFe_{1/2}Mn_{1/2}O_2$ compound is ascribed to the CBH model, while P2-$Na_{2/3}Fe_{1/2}Mn_{1/2}O_2$ can be attributed to the OLPT model.

Received 18th April 2023
Accepted 5th June 2023

DOI: 10.1039/d3ra02570e

rsc.li/rsc-advances

1. Introduction

The layered sodium-transition metal oxides $NaMO_2$ are considered among the most promising cathode materials for Na-ion batteries (NIBs) by providing comparable activity to canonical Li-ion batteries (LIBs).[1–14] Indeed, Na_xMO_2 (M = Fe, Mn, Ni, Cr, and Co, *etc.*), have received much interest and have been extensively explored as outstanding cathode materials for NIBs owing to their high theoretical capacities, high working voltage as well as simple synthesis processes and importantly their structure rearrangement.[15–17] The structure of Na_xMO_2 compounds can be divided into two major groups, O and P type structures, based on the location of sodium ions at either octahedral or prismatic sites, respectively, squeezed between the edge-sharing sheets of [MO_6] octahedra.[17] First, Na_xMnO_2 crystallizes in two structures as described by Parant, *et al.*[18] At low temperature, α-$NaMnO_2$ has an O3 shell structure with a monoclinic structural distortion because of the Jahn–Teller effect of Mn^{3+} ions. However, the orthorhombic β-$NaMnO_2$ crystallizes at high temperature in a unique layered structure containing MnO_2 sheets made up of a double stack of edge-sharing MnO_6 octahedra. The octahedral positions between two adjacent sheets are occupied by Na ions.[19] Second, Tetsuaki Nishida *et al.*[20] reported that $NaFeO_2$ has two polymorphs, namely β phase of orthorhombic symmetry and the α phase of rhombohedral symmetry which is classified as O3-like shell structure according to Delmas notation.[21] In addition, different transition metal elements can be mixed in the transition metal layers to form $Na_xM_{1-y}M'_yO_2$ with enhanced electrochemical properties. In this respect, $NaNi_{1/2}Mn_{1/2}O_2$ provides a discharge capacity of 125 mA g^{-1} between 3.8 V and 2 V, with 75% capacity retention after 50 cycles at 0.2 C, whereas $Na_{2/3}Ni_{1/3}Mn_{2/3}O_2$ delivers a high capacity of 161 mA h g^{-1} with poor cycle stability,[21,22] $NaFe_{1/2}Mn_{1/2}O_2$ provides a capacity of 110 mA h g^{-1} in the potential range of 1.5–4.3 V, whereas $Na_{2/3}Fe_{1/2}Mn_{1/2}O_2$ exhibits a high capacity of 190 mA h g^{-1}.[23] Numerous XRD studies of $NaFe_xMn_{1-x}O_2$ have highlighted the layered structure for these compounds. Basically, $NaFe_xMn_{1-x}O_2$ is characterized by either a P3 layered structure or an O3 layered structure.[22] If Fe : Mn ratio is 1/3 : 2/3 and 1/2 : 1/2, the $NaFe_xMn_{1-x}O_2$ compounds exhibit the P3 shell structure. However if the Fe : Mn ratio is 2/3 : 1/3, the material forms O3 structure.[23] The two samples (for $x = 1$ and 2/3) crystallize in different layered structures. All diffraction peaks of $Na_{2/3}Fe_{1/2}Mn_{1/2}O_2$ are indexed in *xh* a $P6_3/mmc$ space group (hexagonal lattice). These mesh parameters include unit cell lengths $a = b = 2.9154(2)$ Å and $c = 11.2599(1)$ Å, unit cell angles $\alpha = \beta = 90°$ and $\gamma = 120°$. However, the diffraction lines of $NaFe_{1/2}Mn_{1/2}O_2$ are assigned to

[a]*Laboratory LaSCOM, University of Sfax, BP1171, 3000, Sfax, Tunisia. E-mail: abdallahrhaiem@yahoo.fr*

[b]*Department of Chemical Engineering, Engineering Faculty, Sivas Cumhuriyet University, 58140 Sivas, Turkey*

[c]*GREENMAT, CESAM, Institute of Chemistry B6, University of Liège, 4000 Liège, Belgium*

† Electronic supplementary information (ESI) available. See DOI: https://doi.org/10.1039/d3ra02570e

a rhombohedral lattice with space group $R\bar{3}m$, these lattice parameters which include unit cell lengths $a = b = 2:9590(6)$ Å and $c = 16:522(2)$ Å, unit cell angles $\alpha = \beta = 90°$ and $\gamma = 120°$.[23] The P2-$Na_{2/3}Fe_{1/2}Mn_{1/2}O_2$ provides higher discharge capacity at low C-rate of 12 mA g^{-1} in the voltage range of 1.5 to 4.3 V, and about 190 mA h g^{-1}, relative to O3-$NaFe_{1/2}Mn_{1/2}O_2$ which has a discharge capacity of about 105 mA h g^{-1}. This suggests that more Na^+ extraction/insertion occurs through the P2-$Na_{2/3}Fe_{1/2}Mn_{1/2}O_2$structure. Mortemard de Boisse and al have also shown that the O3 phases have discharge capacities of about 135–140 mA h g^{-1}, slightly lower than those of the P2 phases (145–150 mA h g^{-1}).[24] The promising crystal structures and the prominent electrochemical results of these compounds $Na_xFe_{1/2}Mn_{1/2}O_2$ (x = 1 and 2/3) incite us to explore other physical properties of these materials such as vibrational, and electrical properties. Indeed, this type of structure influences the electrical properties of these compounds, in particular the electrical conductivity because the Na^+ charge carrier is free. Moreover, at the band gap between the valence band and the conduction band, which indicates semiconductor behavior, 3d transition metals, are characterized by the overlap between the narrow 3d bands.

In this research work, the layered P3/P2-$Na_xFe_{0.5}Mn_{0.5}O_2$- with x = 1 and 2/3 samples were synthesized and the related atomic structures were carefully investigated using Rietveld refinement. The vibrational study of both compounds was undertaken using IR and Raman spectroscopy. The electrical properties were examined to thoroughly clarify the transport phenomena by combining conductivity and impedance studies. This study provides and demonstrates the convenient model accounting for the conduction mechanism of these materials.

2. Experimental part

$NaFe_{1/2}Mn_{1/2}O_2$ and $Na_{2/3}Fe_{1/2}Mn_{1/2}O_2$,were synthesized using a solid-state process,[23,27] using Na_2CO_3 (Sigma Aldrich, 99%), Fe_2O_3(Sigma Aldrich, 99%), and Mn_2O_3(Sigma Aldrich, 99%) as precursors with the molar ratios of 1 : 1/2 : 1/2 and 2/3 : 1/2 : 1/2, respectively. The precursors were mixed and e thoroughly ground using a mortar and pestle, and then pressed into pellets. The pellets were heated at 700 °C for 36 h for $NaFe_{1/2}Mn_{1/2}O_2$ and 1000 °C for 12 h for $Na_{2/3}Fe_{1/2}Mn_{1/2}O_2$ in air. Subsequently, they were quenched to room temperature and stored in an Ar-filled glove box until use.

In order to confirm the purity of the produced samples, the Bruker D8 Discover Twin-X-ray Twin's diffraction was used on powder at room temperature with Cu Kα radiation (λ = 1.5406 Å, 10°≤ 2θ ≤ 90°). With a 15 kV accelerating voltage and high vacuum, a scanning electron microscope (XL30 FEG ESEM, FEI) was utilized to examine their morphology. A PerkinElmer spectrum 100 FT-IR spectrometer was invested for the IR spectroscopic study, which was conducted in the 350–1200 cm^{-1} spectral region. Raman spectra were measured using a micro-Raman system (Renishaw inVia Qontor, UK) equipped with a 785 nm laser.

Finally, the electric measurements were carried out using the Soltran SI 1260 impedance analyzer in serial mode with an alternate current in the temperature ranges of [333–453 K] and frequency [10^{-1}–10^7 Hz]. Pellets were placed between two electrodes in a customized container and coated on the opposing sides with a thin layer of silver to provide satisfactory contact. Using a 5 t cm^{-2} pressure, the powder was crushed to create a disc that was 8 mm in diameter, 1 mm thick and with an area of 50.24 × 10^{-3} mm^2.

3. Results and discussion

3.1. X-ray diffraction and structural analysis

The X-ray diffraction patterns of the compounds $Na_xFe_{1/2}Mn_{1/2}O_2$ for x = 1 and 2/3 are depicted in Fig. 1. The reflection peaks of $NaFe_{1/2}Mn_{1/2}O_2$ diagram were indexed by trigonal with space group $R\bar{3}m$ (isostructural at α-$NaFeO_2$ (ICSD #187705)) and characterized by a P3 layered structure. It is noteworthy that several traces of $NaFeO_2$ were observed. Furthermore, the $Na_{2/3}Fe_{1/2}Mn_{1/2}O_2$ diagram was indexed by hexagonal lattice with space group $P6_3/mmc$ (PDF# 16-3250), which is isostructural with P2-type Na_xCoO_2. This result is in good agreement with the result reported by Yuliang Cao *et al.*[25] Certain impurity peaks were detected from the diffraction patterns. These impurities correspond to Na_3FeO_3 and Mn_2O_3 phases. Table 1 displays the cell parameters and the refinement parameters. The schematic

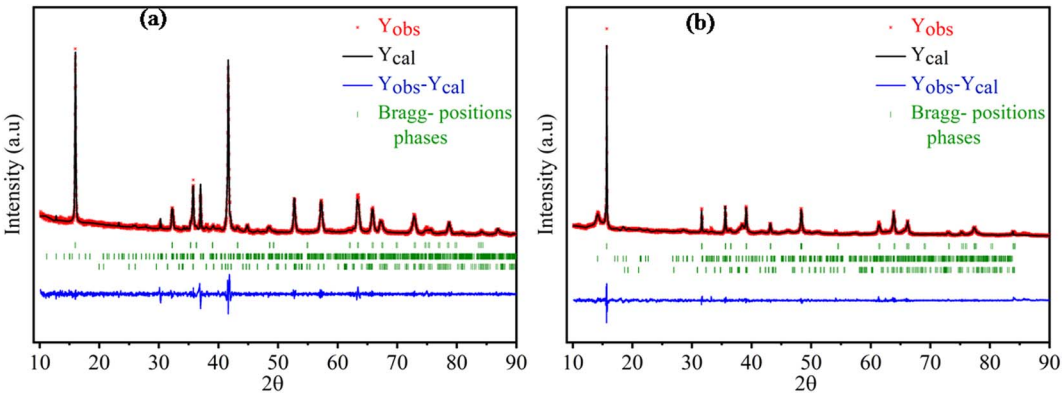

Fig. 1 The Rietveld refinement XRD of synthesized of (a) $Na_{2/3}Fe_{1/2}Mn_{1/2}O_2$, (b) $NaFe_{1/2}Mn_{1/2}O_2$ at room temperature.

Table 1 Crystal data of $NaFe_{1/2}Mn_{1/2}O_2$ and $Na_{2/3}Fe_{1/2}Mn_{1/2}O_2$

Compounds	$NaFe_{1/2}Mn_{1/2}O_2$	$Na_{2/3}Fe_{1/2}Mn_{1/2}O_2$
System	Trigonal	Hexagonal
Space group	$R\bar{3}m$	$P6_3/mmc$
Formula units (Å)	$a = b = 2.9327(2)$	$a = b = 2.918(5)$
	$c = 16.6268(17)$	$c = 11.301(2)$
	$\gamma = 120°$	$\gamma = 120°$
R_B	0.754	1.247
R_f	0.489	1.371
χ^2%	1.43	1.61

diagram of the P3 and P2-structure is provided in Fig. 2(a) and (b). In P2-$Na_{2/3}Fe_{1/2}Mn_{1/2}O_2$, the Na ions in prismatic sites are sandwiched between the MO_2 sheets to form a layered structure. It is clearly observed that the repetitive unit number of MO_2 sheets is 2 and the Na ions in prismatic site have two different types, Na_f (shares face) and Na_e (shares edge), sharing face or edge with MO_6 octahedra, respectively. Both sites are simultaneously occupied by Na ions to minimize electrostatic repulsion between sodium ions.[26] In P3-$NaFe_{1/2}Mn_{1/2}O_2$, the Na^+ ions occupy prismatic sites which share faces and edges with the surrounding MO_6 octahedra.[27] The atomic positions of each sample are illustrated in Table 1S† and the interatomic distances of Na–O and FeMn–O are portrayed in Table 2.

The investigation of the sample morphology and particle size is carried out using the scanning electrode microscope (SEM). The SEM images of the investigated materials are summarized in Fig. 3. The micrographs show the agglomeration of the primary particles, and a Lorentzian fit indicating that the average particle size is 1.088 μm for $x = 1$ and 1.297 μm for $x = 2/3$ (Fig. S1†). Fig. S2† reveals the elemental composition and

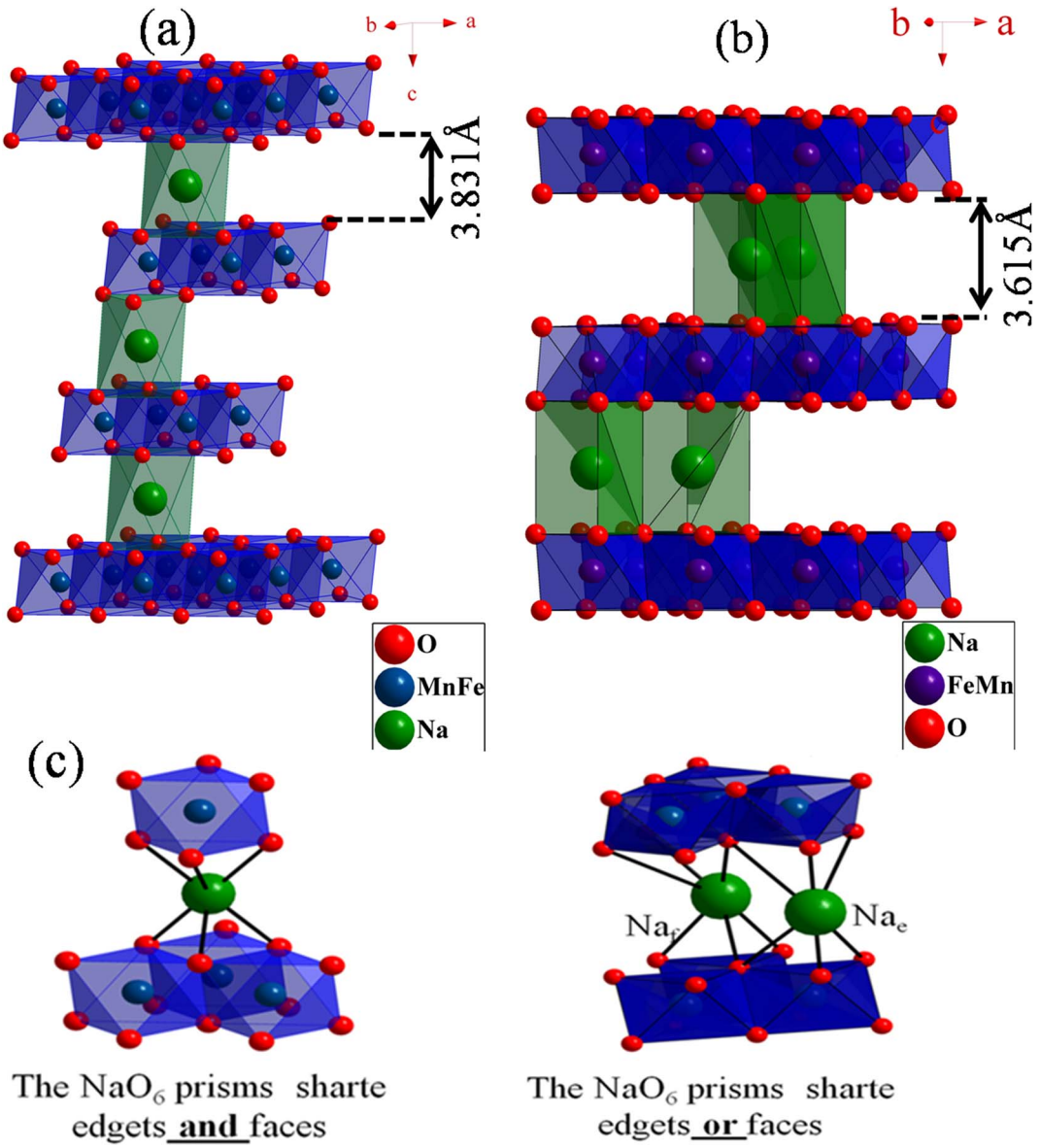

Fig. 2 View of lamellar structure of (a) P3-$NaFe_{1/2}Mn_{1/2}O_2$, (b) P3-$Na_{2/3}Fe_{1/2}Mn_{1/2}O_2$ (c) the Na^+ geometric site in P3 structure *vs.* P2 structure.

Table 2 Interatomic distances

$Na_xFe_{1/2}Mn_{1/2}O_2$	$x = 1$	$x = 2/3$
Na_1–O (Å)	2.412	3.604
Na_2–O (Å)		3.403
MnFe–O (Å)	1.994	2.956
Na_1–Na_2 (Å)		1.664

homogeneity investigated through EDX microanalysis. We infer the homogenous distribution of all elements (Na, Fe, Mn, and O), which is indicative that they are all stable at high temperatures of 700 and 1000 °C for $NaFe_{1/2}Mn_{1/2}O_2$ and $Na_{2/3}Fe_{1/2}Mn_{1/2}O_2$, respectively.

3.2. FTIR and Raman studies

At room temperature, between 350 and 1200 cm^{-1}, the FTIR spectra of $NaFe_{1/2}Mn_{1/2}O_2$ and $Na_{2/3}Fe_{1/2}Mn_{1/2}O_2$ powders were carried out (Fig. 4a). The both spectra confirm the presence of the octahedral groups MO_6 (M = Mn and Fe) in the compounds. Indeed, the observed band at 355 cm^{-1} for both compounds is attributed to the deformation vibration ν_4 (F_{1u}). The weak bands observed at 535 and 684 cm^{-1} for $NaFe_{1/2}Mn_{1/2}O_2$ compound and at 538 and 688 cm^{-1} for $NaFe_{1/2}Mn_{1/2}O_2$ compound correspond to the stretch vibration at ν_3 (F_{1u}). Notably, the stretching vibration of the Na–O band is represented by the peaks detected at about 868 and 904 cm^{-1} for composition $x = 1$ and at 866 and 902 cm^{-1} for $x = 2/3$.[28,29]

Fig. 4b displays the pure Raman spectra in the 100–800 cm^{-1} wave number range of $NaFe_{1/2}Mn_{1/2}O_2$ and $Na_{2/3}Fe_{1/2}Mn_{1/2}O_2$ compounds. Two main bands are found, which is in good consistency with what the results that have been reported in the literature. The elongation vibration is attributed to ν_1 (A_{1g}) observed band at 587 and 613 cm^{-1} for $x = 1$ and $x = 2/3$, respectively. The band observed at 448 cm^{-1} for the compound $NaFe_{1/2}Mn_{1/2}O_2$ and those observed at 469 and 368 cm^{-1} for the compound $Na_{2/3}Fe_{1/2}Mn_{1/2}O_2$ are ascribed to ν_2 (E_g). The distortion vibration assigned to the ν_4 (F_{1u}) band observed at 253 cm^{-1} corroborates the presence of octahedra MO_6 in sample 1. The deformation vibration ν_5 (F_{2g}) observed at 155 cm^{-1} in the compound $NaFe_{1/2}Mn_{1/2}O_2$,[30] can be accounted for in terms of the fact that the vibrational studies at room temperature confirm the octahedral environment MO_6 (M = Fe, Mn) observed in the structural study for these materials.

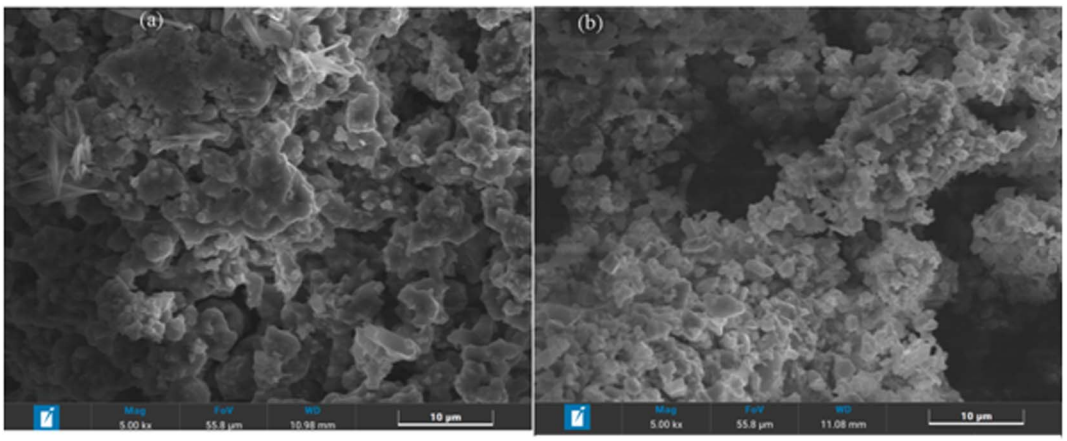

Fig. 3 SEM images, (a) $NaFe_{1/2}Mn_{1/2}O_2$, (b) $Na_{2/3}Fe_{1/2}Mn_{1/2}O_2$.

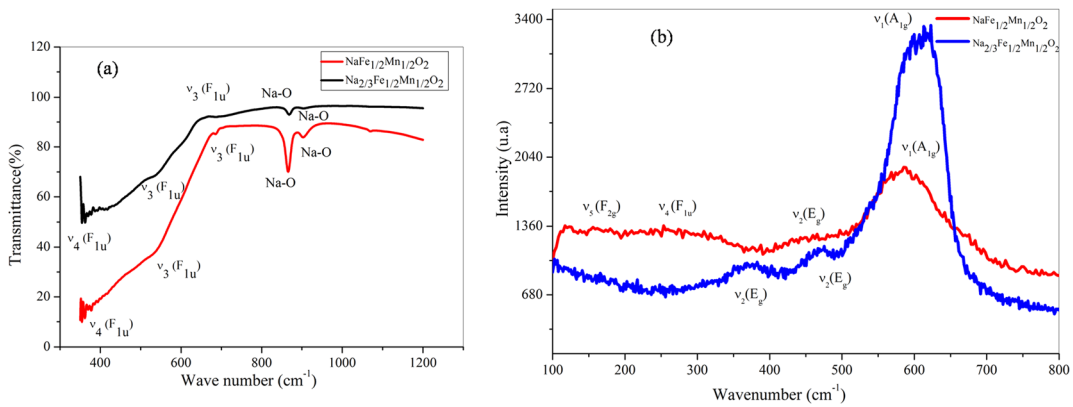

Fig. 4 (a) Fourier transform infrared (FTIR) of $NaFe_{1/2}Mn_{1/2}O_2$ and $Na_{2/3}Fe_{1/2}Mn_{1/2}O_2$. (b) Raman of $NaFe_{1/2}Mn_{1/2}O_2$ and $Na_{2/3}Fe_{1/2}Mn_{1/2}O_2$.

3.3. Dielectric study

Al though multiple reports have focused on lamellar oxide, numerous mechanisms have not been fully investigated to account for the different behaviors of dielectric features. Additionally, in the state of artworks, the dielectric study of these particular lamellar oxides was not fully deciphered and thoroughly addressed.

Impedance spectroscopy stands as one of the most outstanding and powerful tools to investigate the dielectric and electrical properties of these materials in large frequency and temperature ranges. Furthermore, the dependence of dielectric parameters on frequency and temperature can be analyzed as follows[31]

$$\varepsilon = \varepsilon' + i\cdot\varepsilon''$$

where ε stands for the dielectric constant which can be regarded as a complex number. ε' and ε'' indicate the real and imaginary parts of the dielectric constant which refer to the stored energy and the energy dissipation of the applied electric field, respectively. These two parameters can therefore be calculated using the following equations.[31]

$$\varepsilon' = \frac{Z''}{2\pi f C_0 (Z'^2 + Z''^2)}$$

$$\varepsilon'' = \frac{Z'}{2\pi f C_0 (Z'^2 + Z''^2)}$$

where Z' and Z'' express the real and the imaginary parts of the impedance, respectively. f corresponds to the frequency and C_0 refers to the free space capacitance ($C_0 = \frac{\varepsilon_0 A}{d}$ where d is the pellet thickness and A is the area).

Fig. 5a and b illustrate the real (ε') component of the dielectric permittivity for $x = 1$ and $x = 2/3$. It is obvious that lower frequencies have greater values for these dielectric constants.[32] Basically, the capability for storing energy decreases as the ε' value drops at higher frequencies.[33] The Maxwell-interfacial Wagner's polarization may account for the observed dielectric behavior for both compounds. This explanation interpretation is in good accordance with Koop's phenomenological theory of dielectric materials. Relying upon these models, the dielectric structure of the prepared sample is presumed to involve good-conductive grains separated by poor-conductive grain boundaries. The sample grains and grain borders need to be crossed by electrons during the exchange process. The inter-grain conductivity drops refer to the weakening of the electron hopping triggered by the grain boundary.[34,35] We can also infer from Fig. 6a and b that the dielectric constants (ε') rapidly fall at low frequencies before becoming frequency independent at high frequencies. This is in good conformity with previous findings.[36,37] As the electrons in the grain can no longer follow the alternating field, the consistency of (ε') is at high frequencies. Since the electrons hopping are thermally stimulated, it is also detected that ε' increases as the temperature increases.

Such physical phenomena, such as the conduction process, the dielectric relaxation, the interfacial polarization, and the molecular dipole moment, were chiefly responsible for the dielectric loss that quantitatively defined the electrical energy dissipation.[38] The dissipation factor was computed based on the following equation.

$$\tan\delta = \frac{\varepsilon''}{\varepsilon'}$$

where ε' and ε'' are the real and imaginary parts of the dielectric constant (ε*), respectively.

Fig. 6a and b reveal that tan δ has relatively modest values of 1.01–12.69 for both compounds. It is to be noted that materials with little energy loss are needed for possible applications in electronic devices, which makes the compounds $NaFe_{1/2}Mn_{1/2}O_2$ and $Na_{2/3}Fe_{1/2}Mn_{1/2}O_2$ an optimum choice. The dielectric loss factor proved to drop with an increase in frequency. Resting on Koop's theory, existing imperfections or impurities in the material build up a potential barrier for the transportation of the charge carriers. The space charge polarization restricts the partial conduction of charges until they are clogged at a possible barrier or grain boundary. These compounds equally depict two relaxation peaks in a low and a high-frequency region,

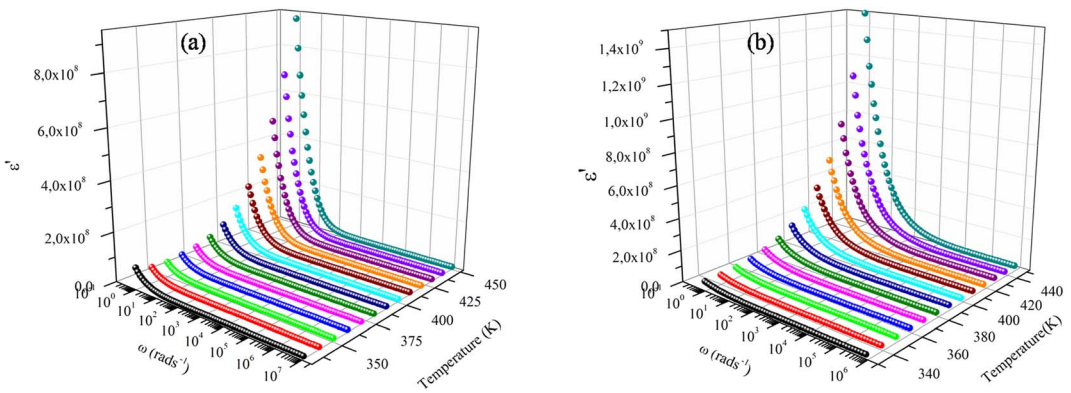

Fig. 5 Dielectric constants of the samples (a) $NaFe_{1/2}Mn_{1/2}O_2$, (b) $Na_{2/3}Fe_{1/2}Mn_{1/2}O_2$ at different temperatures.

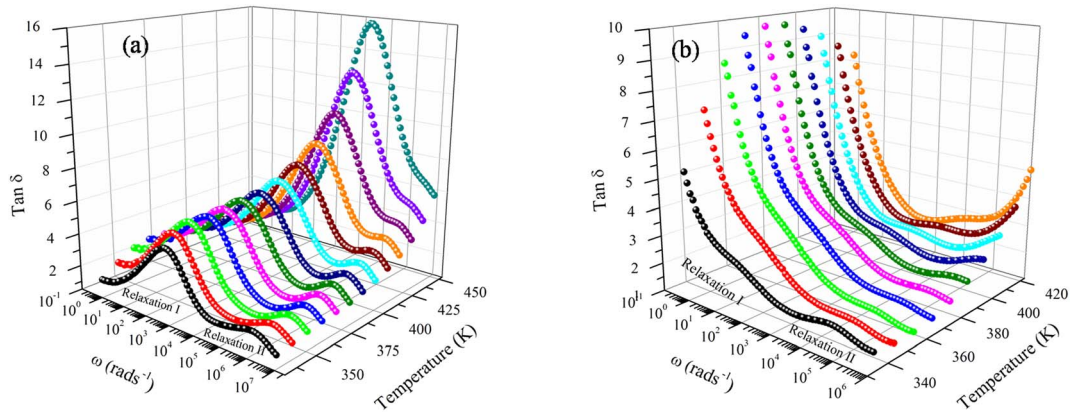

Fig. 6 Frequency-dependent dielectric loss (tan δ) of (a) $NaFe_{1/2}Mn_{1/2}O_2$, (b) $Na_{2/3}Fe_{1/2}Mn_{1/2}O_2$.

respectively. These peaks are indexed for space charge and dipole polarization, respectively. The heights of the relaxation peaks for $x = 1$ are higher than those for $x = 2/3$, while the relaxation peaks for $x = 1$ are found at higher frequencies compared to the peaks for $x = 2/3$. Consequently, tan δ has high values in the lower frequencies zone, and then decreases in the higher frequencies range. The space charge polarization makes it harder for charge carriers to move around in the low frequency domain, requiring additional energy. The values of tan(δ) are hence higher in this frequency range. The material's resistivity drops with frequency, which results in less energy being used by the passage of charge carriers. As a result, the high frequency region's dielectric loss lowers. Additionally, it is evident that tan(δ) gets darker as the temperature increases. It is worthed noting that low energy loss plays a crucial role for the materials in battery applications. In this context, the compound $Na_{2/3}Fe_{1/2}Mn_{1/2}O_2$ is a promising candidate compared to $NaFe_{1/2}Mn_{1/2}O_2$ for such applications.[27]

Fig. 8 outlines the plot of $\ln(\omega_\delta)$ *vs.* $1000/T$ (ω_δ is the angular frequency of grain boundary relaxation). It is noteworthy that the values of ω_δ go down with the increase in temperature, which indicates the thermally activated process. The temperature-dependent characteristics of ω_δ follow the Arrhenius relation, as presented below:

$$\omega_\delta = \omega_0 e^{\left(-\frac{E_a}{K_B T}\right)}$$

where E_a is the activation energy.

The E_a values estimated from the slope of the linear fit plot (see Fig. 7a and b) amount to 0.74 eV ($T > 363$ K) and 0.1 eV ($T < 363$ K) for $NaFe_{1/2}Mn_{1/2}O_2$ and correspond to 0.62 eV for $Na_{2/3}Fe_{1/2}Mn_{1/2}O_2$.

3.4. Electrical impedance spectroscopy

Complex impedance spectroscopy (CIS) stands for a basic and powerful procedure invested to explore the electrical behaviour of the material. It supplies information on the relaxation time electrical conductivity and movement.[40]

The complex frequency-dependent impedance corresponds to a non-destructive technique depicting the electrode contribution, the grain boundary, and the bulk (grain) in the compound when the time-reversed electric field is applied. The charge carrier notably tends to become active and triggers dipole orientation.

Fig. 8 and 9 exhibit Nyquist diagrams of $NaFe_{1/2}Mn_{1/2}O_2$ and $Na_{2/3}Fe_{1/2}Mn_{1/2}O_2$ respectively at different temperatures. The equivalent circuit parameters are foregrounded in Tables 2Sa and b.† The features of these spectra involve three distinct

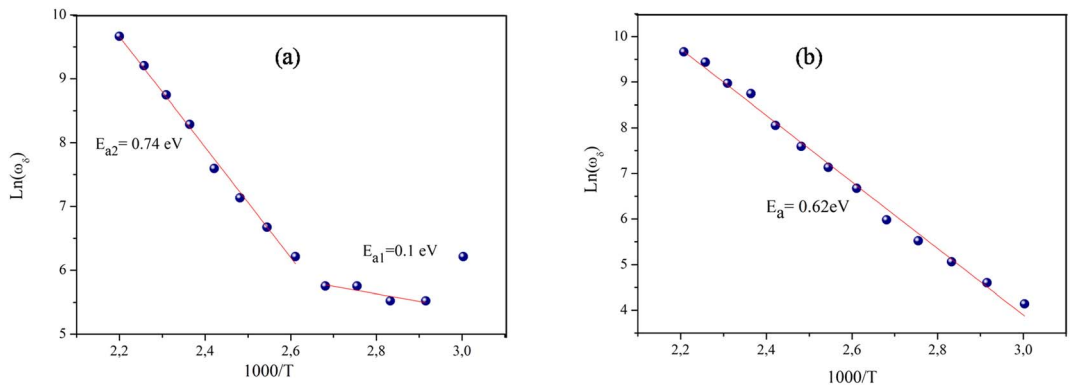

Fig. 7 The variation of $\ln(\omega_\delta)$ *versus* the inverse of temperature (a) $NaFe_{1/2}Mn_{1/2}O_2$, (b) $Na_{2/3}Fe_{1/2}Mn_{1/2}O_2$.

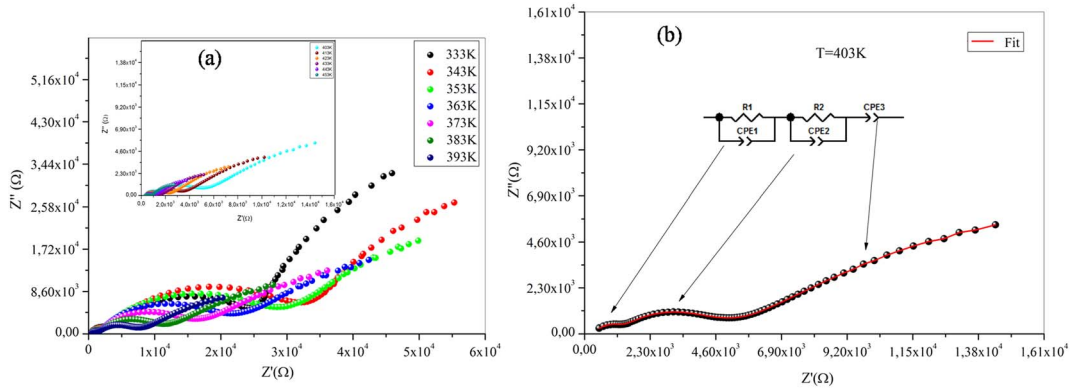

Fig. 8 (a) Nyquist diagrams of $NaFe_{1/2}Mn_{1/2}O_2$ sample, (b) equivalent circuit for $NaFe_{1/2}Mn_{1/2}O_2$ sample.

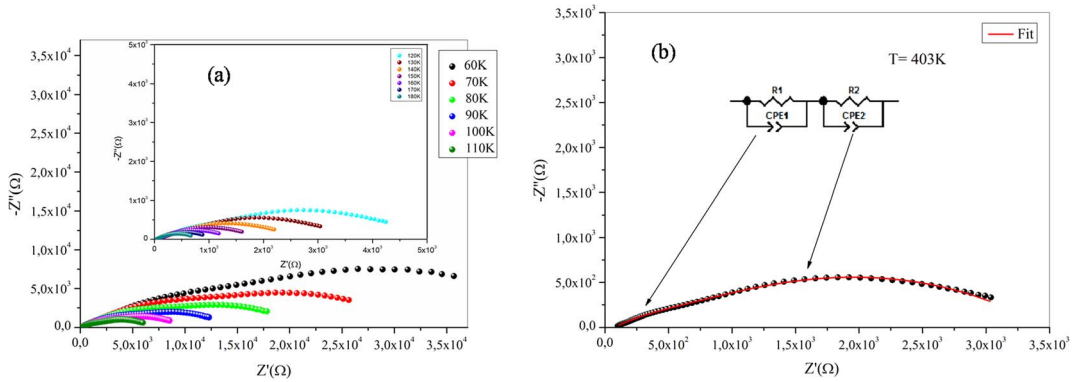

Fig. 9 (a) Nyquist diagrams of $Na_{2/3}Fe_{1/2}Mn_{1/2}O_2$ sample, (b) equivalent circuit for $Na_{2/3}Fe_{1/2}Mn_{1/2}O_2$ sample.

frequency domains, comprising the grain effect, correlated with high frequency, the grain boundary effect, and electrode effect, respectively at medium and low frequency of $NaFe_{1/2}Mn_{1/2}O_2$ compound. However, the $Na_{2/3}Fe_{1/2}Mn_{1/2}O_2$ compound is marked with the two distinct frequency domains, involving the grain effect, correlated with high grain boundary effect at low frequency. Basically, the loss peak occurs when the jump frequency roughly matches the frequency of an applied external AC field. Furthermore, the hopping mechanism indicates that electrical conductivity rises with temperature which causes the thermally activated charge carriers.[37]

The Nyquist diagrams for both compounds indicate that the resistance drops as a function of temperature, which may refer to the improvement of the number of charge carriers and their mobility temperature. Therefore, conductivity rises with the rise in temperature. Such behaviour confirms that the conduction process is thermally activated, hence proving the semiconducting characteristic of samples.

Adapted circuits are those that express the conformity of theoretical and experimental spectra with low error values. In our case, for $NaFe_{1/2}Mn_{1/2}O_2$, the selected equivalent circuit is defined by three cells in series, as displayed in Fig. 8b. The first cell indicates the grain effect, the second stands for the grain boundary effect and the last corresponds to the electrode effect. For the $Na_{2/3}Fe_{1/2}Mn_{1/2}O_2$ sample the selected equivalent circuit is defined by two cells in series, as exhibited in Fig. 9b. The first cell indicates the grain effect and the second represents the grain boundary effect. In Fig. 10, we can infer that the grain and grain boundary resistance values of these compounds drop with increasing temperature, suggesting the behavior of a semiconductor for our samples.[39] In addition, it was found that the values of R_{bg} proved to be higher than those of R_g. This may be assigned to the fact that the atomic arrangement near the grain boundary region is disordered, yielding increased electron scattering.

3.5. AC conductivity

Investigating charge carrier physics not only allows the classification of conduction types but also provides details on conduction modes. Fig. 11a portrays the variation of (σ_{ac}) as a function of ln(ω) of the $NaFe_{1/2}Mn_{1/2}O_2$ sample at different temperatures. We report the existence of three domains, the first at high frequency suggesting the grain effect, the second at medium frequency representing the grain boundary effect and the third at low frequency corresponding to the electrode effect. Notably, two domains, the first at high frequency indicating the grain effect and the second at low frequency suggesting the grain boundary effect, characterize the variation of conductivity as a function of the frequency for the compound $Na_{2/3}Fe_{1/2}Mn_{1/2}O_2$ (Fig. 11b). The low frequency (ln(ω) $\geq$ 4 rad s^{-1}) spike

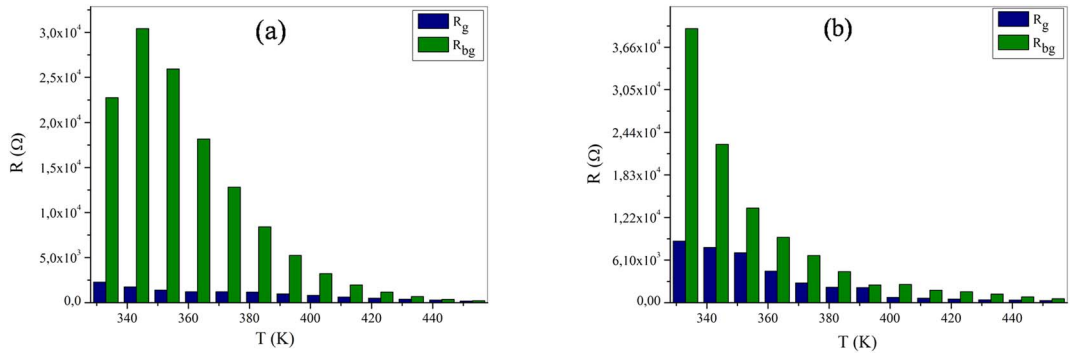

Fig. 10 The variation of (a) R_g, R_{bg} *versus* the temperature for $NaFe_{1/2}Mn_{1/2}O_2$ and (b) R_g, R_{bg} *versus* the of temperature for $Na_{2/3}Fe_{1/2}Mn_{1/2}O_2$.

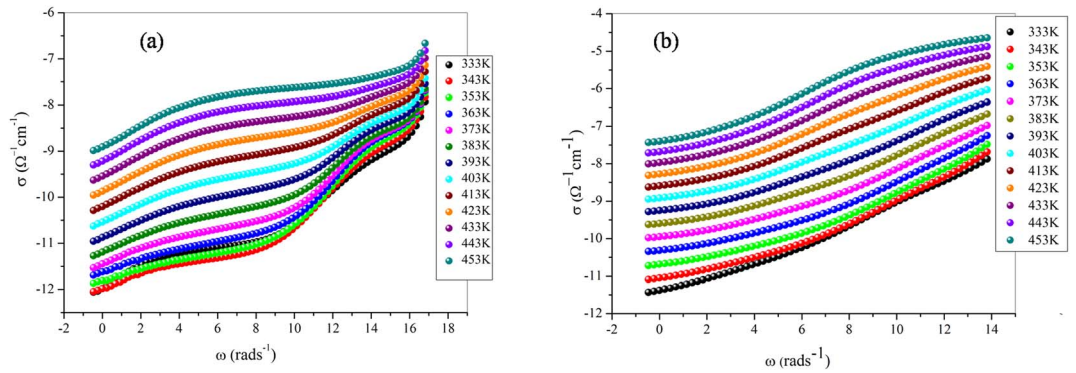

Fig. 11 Frequency dependence of conductivity of the samples (a) $NaFe_{1/2}Mn_{1/2}O_2$, (b) $Na_{2/3}Fe_{1/2}Mn_{1/2}O_2$ *versus* the inverse of temperature.

characterizing electrode–electrolyte interfacial phenomena is assigned to the space charge polarization at the blocking electrodes of $NaFe_{1/2}Mn_{1/2}O_2$ compound. In each frequency domain, the conductivity is estimated relying onJonscher'slaw:[40]

$$\sigma_{ac} = \sigma_{dc} + A\omega^S$$

where σ_{dc} is the sample direct current conductivity, A is a temperature-dependent constant that determines the strength of polarizability and the exponent s is the power law exponent. s is used to identify the interaction between mobile ions with the environments surrounding them where $0 < s < 1$.

The Na^+ ion presents the same high frequency conduction behavior as both compounds exhibit only one high frequency dispersion region. The latter is related to hopping conduction, in which mobile ions can cross barriers more easily when temperature increases. Conductivity proved to be caused by mobile ions (Na^+-ions), depending on their environment. Moreover, the Fe/MnO_6 octahedra exert a significant impact on the mobility of Na^+ ions.

According to Yabuuch N. *et al.* the compounds with higher conductivity have high electrochemical performance. Therefore, the conductivity of $Na_{2/3}Fe_{1/2}Mn_{1/2}O_2$ compound demonstrates almost twice the conductivity of $NaFe_{1/2}Mn_{1/2}O_2$ compound. Thus, we concluded that the variation of sodium content influences the electrochemical performance of the cathode material in sodium-ion batteries.

At the low frequency region, the curves indicate that our samples exhibit semiconducting behaviour in all temperature ranges. The experimental data of dc conductivity are well fitted by the Mott and Davis law, which determines small polaron hopping (SPH) (Fig. 12a and b)[40] in terms of:

$$\sigma_{dc}T = \sigma_0 e^{\left(-\frac{E_a}{K_B T}\right)}$$

where E_a represents the activation energy of the dc-conductivity and σ_0 expresses the pre-exponential factor when the temperature tends to infinite values. These activation energy as obtained from a linear fit of the experimental data are $E_a = 0.2$ eV for $T <$ 363 K and $E_a = 0.53$ eV for $T >$ 363 K of $x = 1$ as a consequence E_a = 0.42 eV of $x = 2/3$. We observe a shift in slope for the $NaFe_{1/2}Mn_{1/2}O_2$ compound approaching $T = 363$ K. At low temperature, a small number of the charge carriers were thermally active and their movement was not the same as that at high temperature. It is noted that both compounds are characterized by the same activation energy at high temperature. For the compound $NaFe_{1/2}Mn_{1/2}O_2$, the doubling of the activation energy at 363 K can be accounted for in terms of a change in the charge carrier (from a small polaron to a large polaron or from a single polaron to a double polaron).

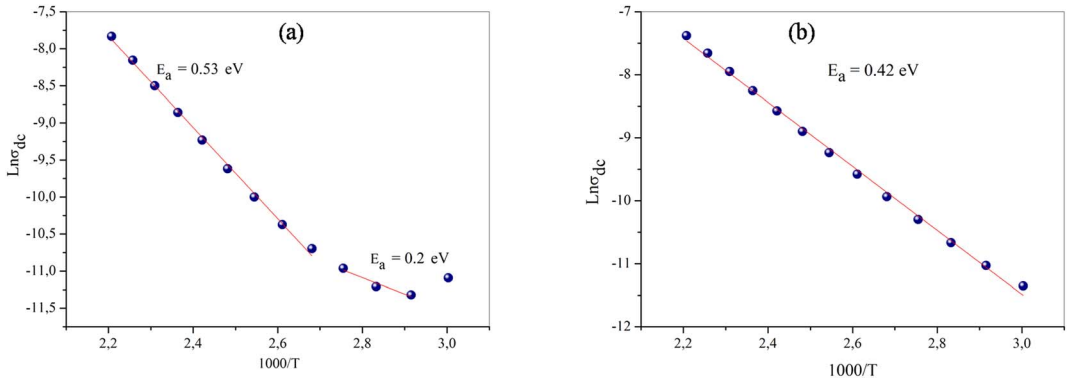

Fig. 12 The variation of ln(σ_{dc}) of the samples (a) $NaFe_{1/2}Mn_{1/2}O_2$, (b) $Na_{2/3}Fe_{1/2}Mn_{1/2}O_2$ *versus* 1000/*t*.

The conductivity value of $Na_{2/3}Fe_{1/2}Mn_{1/2}O_2$ almost doubles that of $NaFe_{1/2}Mn_{1/2}O_2$ referring to the fact that the Na^+ ions are freer in the first compound. Indeed, the Na–O inter-atomic distance in the P2 type structure is equal to 3.604 Å, which is larger than that of P3 structure (2.412 Å). In addition, the mobility of sodium is easier in this structure and therefore the ionic conduction is greater in this compound.

Particularly, when compared to other similar compounds such as $LiCoO_2$, which is the most preferred positive electrode material, an enhancement of conduction in$NaFe_{1/2}Mn_{1/2}O_2$ and $Na_{2/3}Fe_{1/2}Mn_{1/2}O_2$ was recorded. Indeed, at room temperature $LiCoO_2$ has conductivity of 2.29×10^{-4} $(\Omega\ cm)^{-1}$,[41] which is lower than that of $NaFe_{1/2}Mn_{1/2}O_2$ and $Na_{2/3}Fe_{1/2}Mn_{1/2}O_2$, whose conductivities are 4.62×10^{-4} and 9.32×10^{-4} $(\Omega\ cm)^{-1}$, respectively. Thus, $Na_{2/3}Fe_{1/2}Mn_{1/2}O_2$ is a viable option and potential cathode candidate for Na ion batteries.

To gain a deeper and better insight into the change in the activation energy at 363 K for $NaFe_{1/2}Mn_{1/2}O_2$ compound and the increase in conductivity by the reduction in the rate of sodium (x), undertaking a study of the mechanism of conduction in these materials is intrinsic.

The originality as well as the main contribution of our study lies basically in extracting of our study different s values for different relaxation processes. The variation of s_1 (the power law exponent which corresponds to the grain boundary) and s_2 (the power law exponent which corresponds to the grain) for the compound $NaFe_{1/2}Mn_{1/2}O_2$ is plotted in Fig. 13a and b. The exponent s_1 increases in the temperature range 333–363 K and then decreases (low value $s_1 < 0.5$) at the beginning of the temperature 363 K, which confirms that the grain boundary conduction mechanism changes from the non-overlapping small polaron tunneling (NSPT) to the overlapping large-polaron tunneling model (OLPT) model.[42,43] The exponent s_2 decreases with temperature and lies between 0.65 and 0.95, indicating that the grain conduction phenomenon in this material corresponds to the correlated barrier hopping (CBH) model.[42] As far as this model is concerned, the exponent (s) can be identified by the following relation: $s = 1 - \frac{6K_BT}{W_M}$.[42] It is clear that there is a change of slope in the variation of s. Fitting the curve of s through the use of this equation allows to calculate the energy for self-trapping W_M (Fig. S3†). The value of $W_{M2} = 0.42$ eV for $T > 363$ is the double of $W_{M1} = 0.18$ eV for $T < 363$ K, which proves that there is a transition from a CBH model of a single polaron at low temperature to a CBH model of double polaron for $T > 363$ K.[42] Fig. 13c and d portray the variation of s_1 and s_2 of the compound $Na_{2/3}Fe_{1/2}Mn_{1/2}O_2$. The coefficient $s_1$which corresponds to the grain boundary decreases, increases to a great extent according to the temperature and the one which corresponds to the grain (s_2) decreases according to the temperature and it is lower than 0.32. According to Elliott,[43] the OLPT is the most appropriate model in both frequency domains.

Since the frequency dependence of conductivity is important for exploring the mechanism of conduction, the temperature dependence of conductivity is equally fundamental to trace the evolution of the CBH and OLPT models at the grain level in both compounds. Fig. S4a.† demonstrates the variation of AC conductivity as a function of the inverse of the temperature at different frequencies. The correlated barrier hopping corresponds to a model of electron transfer by thermal activation over the barrier between two sites, each displaying a coulombic potential associated related to it. The good accordance between the experimental data and the theoretical calculation fit corroborated that the CBH model characterizes well the behavior of the $NaFe_{1/2}Mn_{1/2}O_2$ sample well, allowing a better estimation of the parameters according to the equation.[44]

$$\delta_{AC} = \frac{n\pi^2 NN_P \varepsilon' R_\omega{}^6}{24}$$

where n refers to the number of polaron involved in the hopping process, NN_p is proportional to the square of the concentration of states and ε' stands for the dielectric constant for a fixed frequency value. The hopping can be indicated by a single polaron or by a bipolaron, where:

$$NN_p = N_T{}^2 \text{ (for bipolar hopping)}$$

$$NN_p = N_T{}^2 e^{\frac{-U_{eff}}{2K_BT}} \text{(for single polaron)}$$

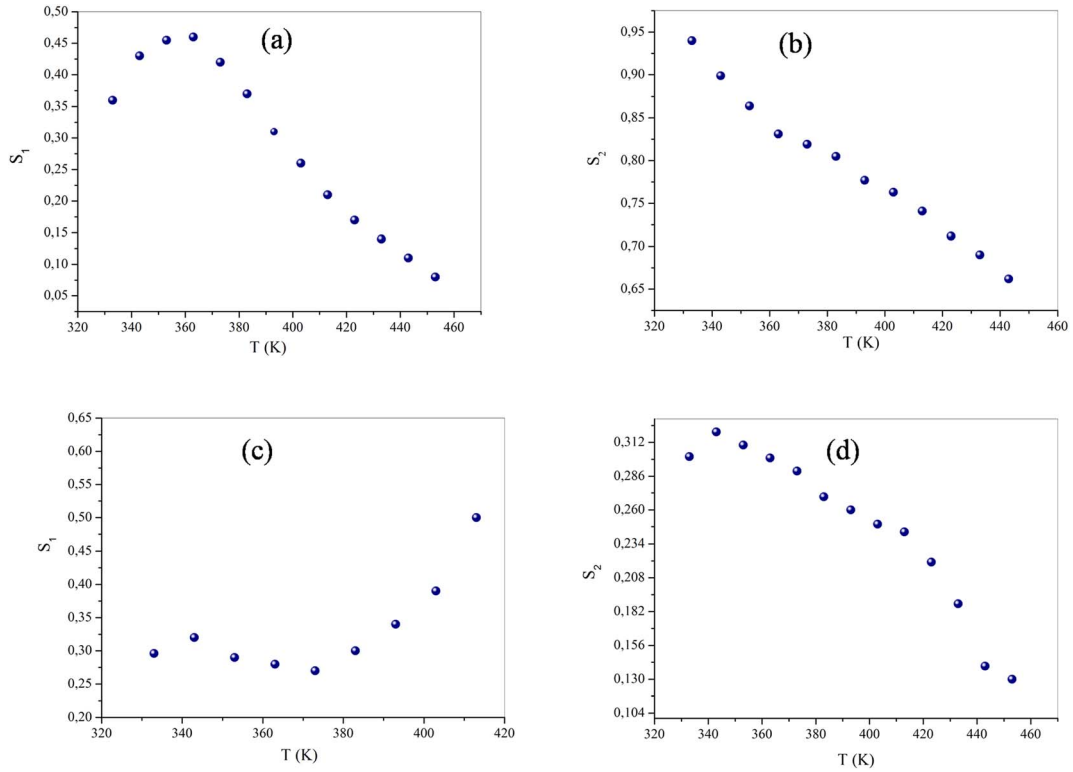

Fig. 13 The variation of the exponent s (a and c) grain boundary, (b and d) grain of $NaFe_{1/2}Mn_{1/2}O_2$ and $Na_{2/3}Fe_{1/2}Mn_{1/2}O_2$ of compounds respectively as a function of temperature.

The hopping length R_ω is determined by the expression:

$$R_\omega = \frac{4ne^2}{\pi\varepsilon'\varepsilon_0[W_M + K_B T \ln(\omega\tau_0)]}$$

where W_M stands for the height of the maximum barrier, whose value drops to a value ω, provided in the case of a single polaron by the following expression:

$$W = W_M - \frac{e^2}{\pi\varepsilon'\varepsilon_0 R}$$

The multiple parameters invested in the fitting procedure are outlined in Tables 3Sa and b.† The negative sign of the effective energy for the single polaron CBH model is associated with the strong interaction between electron and photon. Fig. 14 reveals that the density states decrease with increasing frequency, which is quite expected since the frequency increase stimulates the mobility of the charge carriers, indicating their non-localization.

Fig. S4b† exhibits the variation of $\ln(\sigma_{ac})$ conductivity as a function of the inverse of temperature for $Na_{2/3}Fe_{1/2}Mn_{1/2}O_2$ sample. These curves are fitted using the following expression which corresponds to the OLPT model:[45]

$$\sigma_{ac}(\omega) = \frac{\pi^4}{12}e^2(kT)^2N^2(E_F)\frac{\omega {R_\omega}^4}{2\alpha kT + \frac{\omega_{H_0 r_p}}{{R_\omega}^2}}$$

where $R_\omega$is the intersite separation, r_p is the radius of the large polaron, and ω_{H_0} is denoted by

$$\omega_{H_0} = \frac{e^2}{4\varepsilon_p r_p}$$

where ε_p is the effective dielectric constant and the tunneling distance for a fixed frequency that can be computed with reference to the equation:

$$R_\omega = \frac{1}{4\alpha}\left[\ln\left(\frac{1}{\omega\tau_0}\right) - \frac{\omega_{H_0}}{K_B T}\right] + \left[\left[\ln\left(\frac{1}{\omega\tau_0}\right) - \frac{\omega_{H_0}}{KT}\right]^2 + \frac{8\alpha r_p \omega_{H_0}}{KT}\right]^2$$

where $N(E_F)$ represents the density of the contained state, τ_0 indicates the relaxation time considered as a constant of the order of 10^{-13} sin numerous prior works, ω_{H_0} expresses the activation energy related to the transfer of charge between the overlapping sites, K_B is the Boltzmann constant, r_p refers to the radius of the polaron and R_ω stands for the distance of the tunnel polarons.

These expressions were used in order to better and deeper understand the changes occurring in the material when this model takes place. However, in the OLPT model (Table 4S†), the increase of the frequency entails the decrease of the density of the charge carrier N_T (Fig. 14c), the polaron radius r_p and its hopping energy ω_{H_0}. This indicates that the increase in frequency stimulates the mobility of the charge carrier and triggers the reduction of the polaron radius and therefore its hopping energy.[46,47]

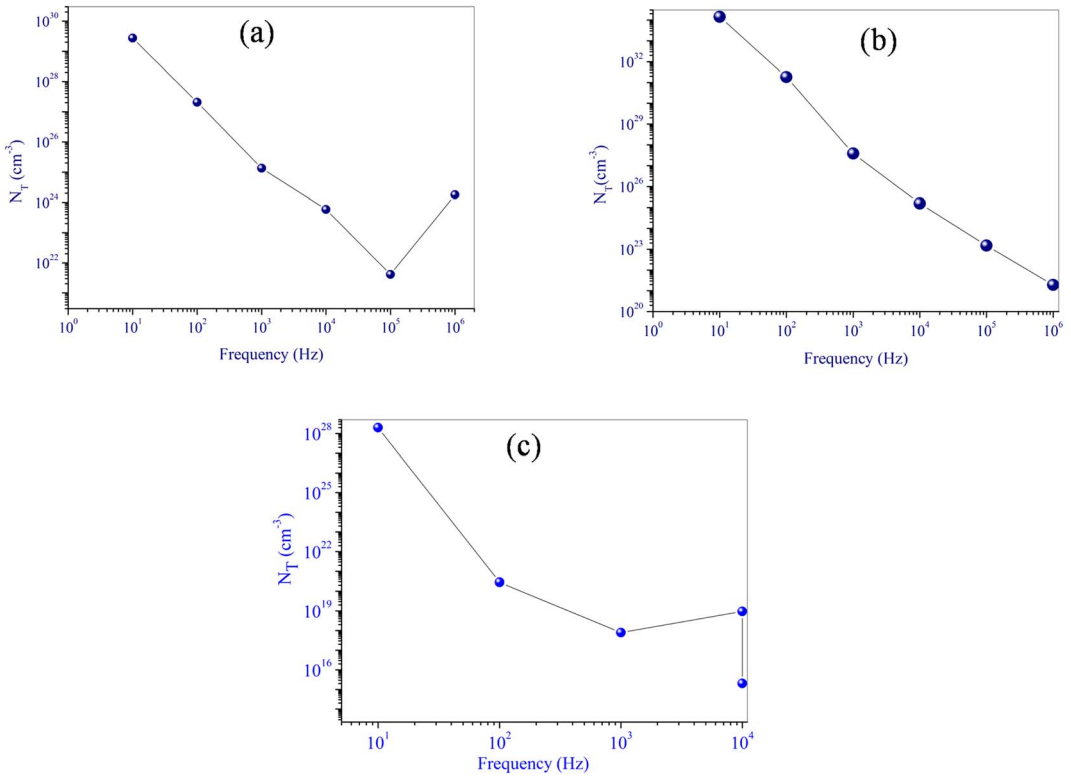

Fig. 14 Frequency dependency of the density states N_T for $NaFe_{1/2}Mn_{1/2}O_2$ (a) single polaron (b) bipolaron (c) $Na_{2/3}Fe_{1/2}Mn_{1/2}O_2$.

In the current research work, we proved that the environment of Na in the materials $Na_xFe_{1/2}Mn_{1/2}O_2$ ($x = 1$ and 2/3) impacts the conduction model. For $x = 1$, the structure is of P3 type, where Na^+ occupies prismatic sites which share faces and edges with the octahedra MO_6. The conductivity obeys, therefore, the jump model. However, for $x = 2/3$, the structure is of P2 type, where Na^+ occupies prismatic sites which share only the edges with the octahedra MO_6. The conductivity obeys, therefore, the tunnel model. Indeed, the height of the NaO_6 prism in the P2 structure is higher than that in the P3 structure, which gives rise to the tunnel model (OLPT) in the compound $Na_{2/3}Fe_{1/2}Mn_{1/2}O_2$.

5. Conclusion

In this work, we successfully synthesized $Na_xFe_{1/2}Mn_{1/2}O_2$ samples ($x = 1$ and 2/3) using a solid state method. We confirmed that the compounds present hexagonal and rhombohedral lattices, with $R\bar{3}m$ and $P6_3/mmc$ space groups, respectively, for $x = 1$ and 2/3. Therefore the compound $NaFe_{1/2}Mn_{1/2}O_2$ has a P3 type structure, while the compound $Na_{2/3}Fe_{1/2}Mn_{1/2}O_2$ has a P2 type structure. The presence of the MO_6 group in these materials was confirmed by the FTIR and Raman vibration spectra. SEM analysis reveals that these samples have a homogeneous morphology with regularly shaped grains. The analysis of complex impedance measurements proved the presence of grain and grain boundary effects for both compounds. The study of dielectric and conductivity σ_{dc} of $NaFe_{1/2}Mn_{1/2}O_2$ compound demonstrated a change in activation energy at $T = 363$ K, which is confirmed by a change in conduction mechanism. We found that the values of the dielectric loss for $x = 2/3$ are lower than those for $x = 1$. It has been found that the grain conduction mechanism in these materials is dependent on the sodium environment. It is of the CBH type in the P3 structure and of the OLPT type in the P2 structure. It is inferred for both compounds that the density states decrease with increasing frequency, which is expected since increasing frequency stimulates the mobility of charge carriers, indicating their non-localization.

Conflicts of interest

The authors declare that they have no known competing financial interests or personal relationships that could have appeared to influence the work reported in this paper.

References

1 N. Yabuuchi, K. Kubota, M. Dahbi and S. Komaba, *Chem. Rev.*, 2014, **114**, 11636–11682.
2 A. Tripathi, S. Xi, R. S. Gajjela and P. Balaya, *Chem. Commun.*, 2020, **56**(73), 10686–10689, DOI: **10.1039/d0cc03701**.
3 Y. Sui, Y. Hao, X. Zhang, J. Li, G. Wen, S. Zhong, Z. Zhang and L. Wu, *Ceram. Int.*, 2021, **47**(4), 5227–5234, DOI: **10.1016/j.ceramint.2020.10.102**.
4 Z. Shadike, E. Zhao, Y. N. Zhou, *et al*, Advanced characterization techniques for sodium-ion battery studies, *Adv. Energy Mater.*, 2018, **8**, 1702588.

5 M. Fehse, D. Bessas, A. Mahmoud, A. Diatta, R. P. Hermann, L. Stievano and M. T. Sougrati, *Batteries Supercaps*, 2020, **3**, 1341–1349.
6 P. K. Nayak, L. Yang, W. Brehm and P. Adelhelm, *Angew. Chem., Int. Ed.*, 2018, **57**, 102–120.
7 Y. Lia, Y. Lu, C. Zhao, Y. S. Hu, M. M. Titirici, H. Li, X. Huang and L. Chen, *Energy Storage Mater.*, 2017, **7**, 130–151.
8 Y. Lu, C. Zhao, X. Qi, Y. Qi, H. Li, X. Huang, L. Chen and S. Y. Hu, *Adv. Energy Mater.*, 2018, **8**(27), 1800108, DOI: 10.1002/aenm.201800108.
9 Y. Li, Y. Lu, C. Zhao, S. Y. Hu, M. M. Titirici, H. Li, X. Huang and L. Chen, *Energy Storage Mater.*, 2017, **7**, 130–151, DOI: 10.1016/j.ensm.2017.01.002.
10 R. Berthelot, D. Carlier and C. Delmas, Electrochemical Investigation of the P2— Na_xCoO_2 Phase Diagram, *Nat. Mater.*, 2011, **10**(1), 74–80.
11 M. Guignard, C. Didier, J. Darriet, P. Bordet, E. Elkaïm and C. Delmas, P2- Na_xVO_2 System As Electrodes for Batteries and Electron-Correlated Materials, *Nat. Mater.*, 2013, **12**(1), 74–80.
12 X. Ma, H. Chen and G. Ceder, Electrochemical Properties of Monoclinic $NaMnO_2$, *J. Electrochem. Soc.*, 2011, **158**(12), A1307–A1312.
13 D. Yuan, X. Liang, L. Wu, Y. Cao, X. Ai, J. Feng and H. Yang, A Honeycomb-Layered $Na_3Ni_2SbO_6$, A High-Rate and Cycle-Stable Cathode for Sodium-Ion Batteries, *Adv. Mater.*, 2014, **26**(36), 6301–6306.
14 I. Hasa, D. Buchholz, S. Passerini and J. Hassoun, A Comparative Study of Layered Transition Metal Oxide Cathodes for Application in Sodium-Ion Battery, *ACS Appl. Mater. Interfaces*, 2015, **7**(9), 5206–5212.
15 J. Li, S. L. Glazier, J. Paulsen, J. R. Dahn, X. Ma and J. Harlow, *J. Electrochem. Soc*, 2018, **165**, 3195–3204.
16 C. Fang, Y. Huang, W. Zhang, J. Han, Z. Deng, Y. Cao and H. Yang, *Adv. Energy Mater.*, 2016, **6**, 5.
17 C. Delmas, C. Fouassier and P. Hagenmuller, *Physica B+C*, 1980, **99**, 81–85.
18 J. P. Parant, R. Olazcuaga, M. Devalette, C. Fouassier and E. T. P. Hagenmuller, *J. Solid State Chem.*, 1971, **3**, 1.
19 S. Kikkawa, S. Miyazaki and M. Koizumi, *J. Power Sources*, 1985, **14**, 231.
20 J. Zhao, L. Zhao, N. Dimov, S. Okada and T. Nishida, *J. Electrochem. Soc.*, 2013, **160**(5), A3077–A3081.
21 C. Delmas, C. Fouassier and P. Hagenmuller, *Physica B+C*, 1980, **99**, 81.
22 X. Lu, Y. Wang, P. Liu, L. Gu, Y. S. Hu, H. Li, G. P. Demopoulos and L. Chen, Direct imaging of layered O3-and P2-$Na_xFe_{1/2}Mn_{1/2}O_2$ structures at the atomic scale, *Phys. Chem. Chem. Phys.*, 2014, **16**(40), 21946–21952.
23 N. Yabuuchi, M. Kajiyama, J. Iwatate, H. Nishikawa, S. Hitomi, R. Okuyama, R. Usui, Y. Yamada and S. Komaba, P2-type $Na_x[Fe_{1/2}Mn_{1/2}]O_2$ made from earth-abundant elements for rechargeable Na batteries, *Nat. Mater.*, 2012, **11**(6), 512–517.
24 B. Mortemard de Boisse, D. Carlier, M. Guignard and C. Delmas, *J. Electrochem. Soc.*, 2013, **160**, A569–A574.
25 B. D. Yuan, X. Hu, J. Qian, F. Pei, F. Wu, R. Mao, X. Ai, H. Yang and Y. Cao, *Electrochim. Acta*, 2014, **116**, 300–305.
26 C. Delmas, C. Fouassier and P. Hagenmuller, *Physica B Condens.*, 1980, **99**, 81.
27 I. Ben Slima, K. Karoui, A. Mahmoud, F. Boschini and A. Ben Rhalem, Structural, optical, electric and dielectric characterization of a $NaCu_{0.2}Fe_{0.3}Mn_{0.5}O_2$ compound, *RSC Adv.*, 2022, **12**, 1563.
28 S. Singh, A. Kumar, T. Gurmeet and S. Lotey, Optical and Luminescence Properties of b-$NaFeO_2$Nanoparticles, *Electron. Mater. Lett.*, 2018, **14**, 594–596, DOI: 10.1007/s133910180067-5.
29 K. Nakamoto, *Infrared and Raman Spectra of Inorganic and Coordination Compounds, Part A: Theory and Applications in Inorganic Chemistry*, J. Wiley, S. Inc, 6th edn, 2009.
30 Wiley and S. Ltd, *Handbook of Vibrational Spectroscopy*, 2006.
31 R. Kalthoum, M. Ben Bechir, A. Ben Rhaiem and M. Gargouri, *Phys. Status Solidi*, 2021, **218**, 2100485.
32 F. Hcini, S. Hcini, B. Alzahrani, S. Zemni and M. L. Bouazizi, *J. Mater. Sci.: Mater. Electron.*, 2020, **31**, 14986.
33 F. Hcini, S. Hcini, B. Alzahrani, S. Zemni and M. L. Bouazizi, *Appl. Phys. A*, 2020, **126**, 362.
34 K. W. Wagner, *Ann. Phys.*, 1913, **40**, 817.
35 C. G. Koops, *Phys. Rev.*, 1951, **83**, 121.
36 S. Hcini, A. Omri, M. Boudard, M. L. Bouazizi, A. Dhahri and K. Touileb, *J. Mater. Sci.: Mater. Electron.*, 2018, **29**, 6879.
37 M. Ben Bechir and M. H. Dhaou, *Mater. Res. Bull.*, 2021, **144**, 111473.
38 P. Sengupta, P. Sadhukhan, A. Ray, R. Ray, S. Bhattacharyya and S. Das, *Appl. Phys.*, 2020, **127**, 204103.
39 K. Trabelsi, K. Karoui, F. Jomni and A. Ben Rhaiem, *J. Alloys Compd.*, 2021, **867**, 159099.
40 M. Ben Bechir and A. Ben Rhaiem, *Phys. E*, 2021, **130**, 114686.
41 B. Nageswara Rao, M. Venkateswarlu and N. Satyanarayana, *Ionics*, 2014, **20**, 175.
42 M. Krimi, K. Karoui, J. J. Suñol and A. B. Rhaiem, *Phase Transitions*, 2019, **92**, 737.
43 I. Ben Slima, K. Karoui, A. Mahmoudb, F. Boschini and A. Ben Rhaiem, *J. Alloys Compd.*, 2022, **920**, 166002.
44 M. Krimi, K. Karoui, J. J. Suñol and A. B. Rhaiem, Optical and electrical properties of Li_2WO_4compound, *Phase Transitions*, 2019, 1639701, DOI: 10.1080/01411594.
45 M. Krimi, K. Karoui, J. J. Suñol and A. Ben Rhaiem, Phase transition, impedance spectroscopy and conduction mechanism of $Li_{0.5}Na_{1.5}WO_4$material, *Phys. E*, 2018, **102**, 137.
46 W. Nasr and A. Ben Rhaiem, Ferroelectric properties and alternative current conduction mechanisms of lithium rubidium molybdate, *Ionics*, 2019, **25**, 4003.
47 W. Ben Nasr, A. Mahmoud, F. Boschini and A. Ben Rhaiem, Optical and AC conductivity studies on $Li_{2-x}Rb_xMoO_4$ (x= 0, 0.5, 1) compounds, *J. Alloys Compd.*, 2019, **522**, 788.